The initial stages of dam-break flow†

By P. K. S T A N S B Y[1], A. C H E G I N I[1] AND T. C. D. B A R N E S[2]

[1] Hydrodynamics Research Group, School of Engineering, The University,
Manchester M13 9PL, UK

[2] School of Mathematics, University of Bristol, Bristol BS8 1TW, UK

Experiments have been undertaken to investigate dam-break flows where a thin plate separating water at different levels is withdrawn impulsively in a vertically upwards direction. Depth ratios of 0, 0.1 and 0.45 were investigated for two larger depth values of 10 cm and 36 cm. The resulting sequence of surface profiles is shown to satisfy approximately Froude scaling. For the dry-bed case a horizontal jet forms at small times and for the other cases a vertical, mushroom-like jet occurs, none of which have been observed previously. We analyse the initial-release problem in which the plate is instantaneously removed or dissolved. Although this shows singular behaviour, jet-like formations are predicted. Artificially smoothing out the singularity enables a fully nonlinear, potential-flow computation to follow the jet formation for small times. There is qualitative agreement between theory and experiment.

In the experiments, after a bore has developed downstream as a result of highly complex flow interactions, the surface profiles agree remarkably well with exact solutions of the shallow-water equations which assume hydrostatic pressure and uniform velocity over depth.

1. Introduction

Dam-break flows are an important practical problem in civil engineering and their prediction is now a required element in the design of a dam and its surrounding environment. The idealized two-dimensional problem of the instantaneous removal of a barrier between two bodies of water at rest with different levels above a horizontal bed has long been a test case for numerical simulations. This is probably because analytical solutions exist if the assumption of hydrostatic pressure is made so that the problem reduces to a one-dimensional problem. This may be generalized to a two-dimensional horizontal plane problem to provide the basis for practical numerical simulations. The equations are known as the shallow-water equations. Simulations based on the full Navier–Stokes/continuity equations have also been made, where the surface is tracked through a fixed mesh, either using particles (the marker-and-cell method), e.g. Harlow & Welch (1965) and Nichols & Hirt (1971), or through surface water concentrations (the volume-of-fluid method), e.g. Hirt & Nichols (1981). The results, at least in terms of the variation of depth profiles with time, have appeared broadly similar to those for the shallow-water solutions.

In practice the release of water will be more gradual than this idealization and depend on water/soil interaction or concrete fracture at a breach. However the

† This article first appeared in volume 370, pp. 203–220 but without p. 213. This reprinting replaces that version and it will be the one that is referenced.
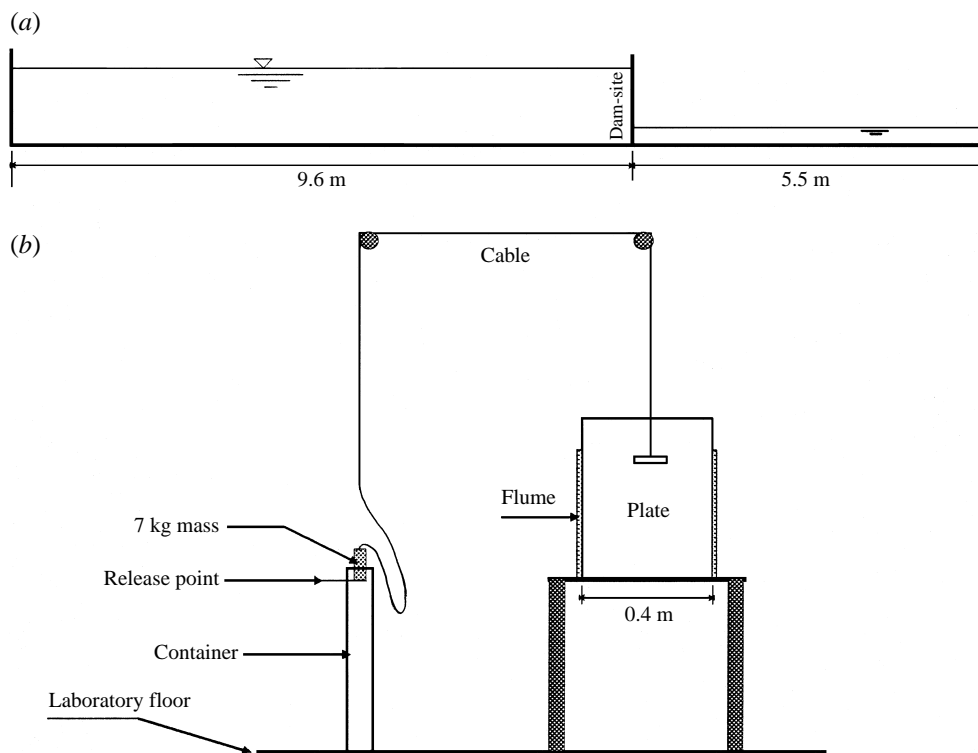
(*a*)

(*b*)

FIGURE 1. Sketch of experimental arrangment: (*a*) side view;
(*b*) section showing pulley/weight system.

instantaneous release may be expected to give the worst case scenario and is therefore a situation of practical, as well as fundamental, interest.

There has been relatively little experimental or theoretical investigation of the initial stages just after release. Here we study the problem experimentally at two different scales in a horizontal channel of rectangular section; a vertical flat plate separating the two levels of water is suddenly withdrawn (upwards). The instantaneous release is then analysed theoretically and some very accurate free-surface computations are made for small times, based on a time-stepping boundary-integral method valid for potential flow. Finally the experimental results are compared with solutions of the shallow-water equations.

2. Experiment

The experiment was conducted in a flume 15.24 m long, 0.4 m wide and 0.4 m high with a horizontal bed, shown in figure 1. Clear Perspex walls were used upstream and downstream of the dam site to view the flow. Both ends of the flume could be closed and the dam site was set up 9.76 m downstream of one end. The dam itself was a thin metal plate, 3 mm thick, which could slide in small plastic channels mounted at a section around the flume bed and sides. Some grease was added to the channels to minimize leakage. A wire rope was attached to the top of the plate; the rope was drawn over a pulley about 3 m above the ground with a 7 kg weight attached to the other end. With the plate in position and the rope taut, the weight is close to the
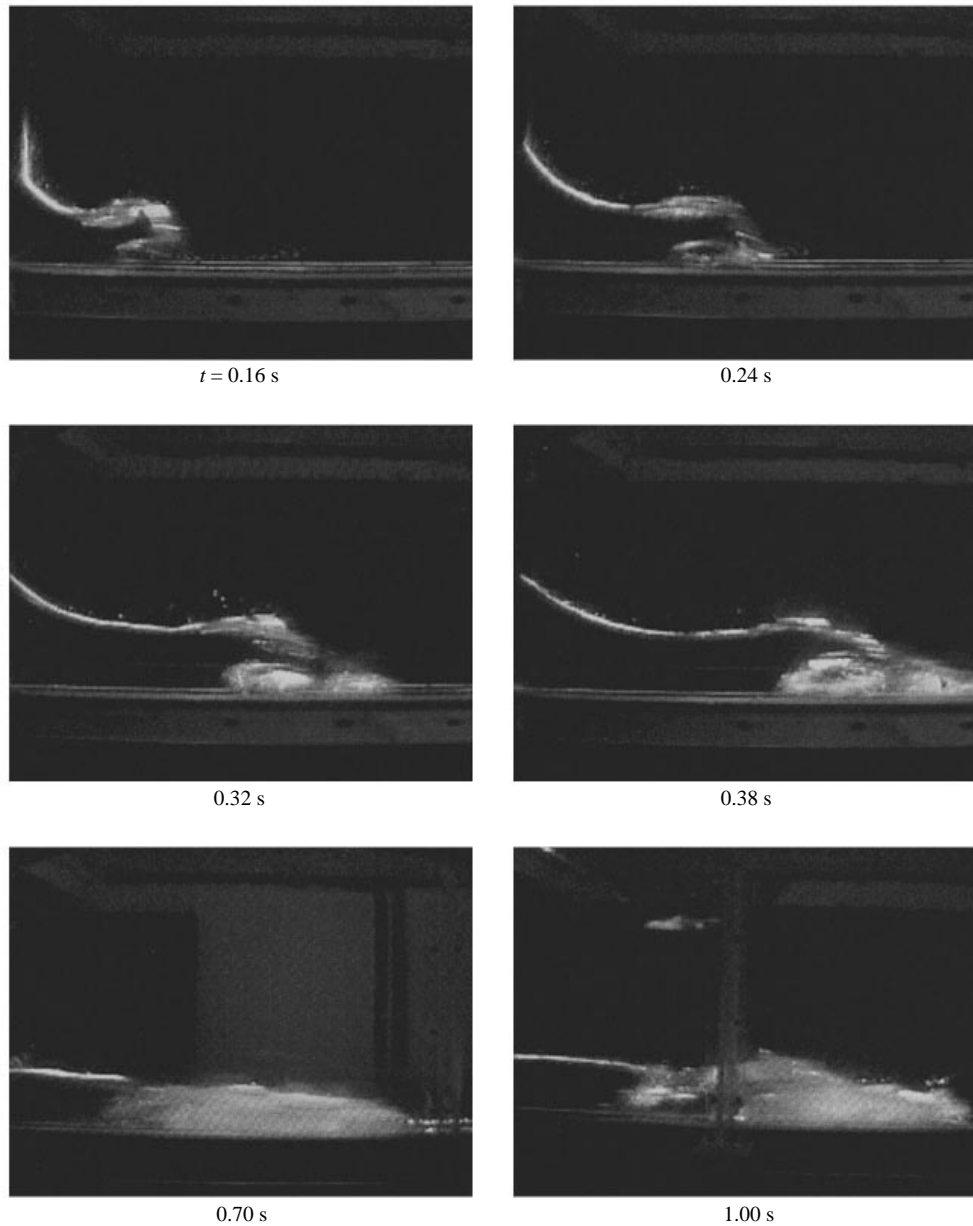
(*a*)

FIGURE 2 (*a*). For caption see p. 412.

ground. An upward impulse is generated by raising the weight and releasing it, with the rope slack, when it is 0.8 m above the ground.

The flow is visualized by a laser light sheet produced by a 4 W argon-ion laser with a fibre-optic cable which directs the beam above the flume through a lens to produce a vertical plane light sheet along the flume at about 7 cm from the near flume wall. The width of the sheet is 1–3 mm. The flow is recorded on a CCD video camera giving a field of view of about 0.83 m height and 1.0 m length. The video images are
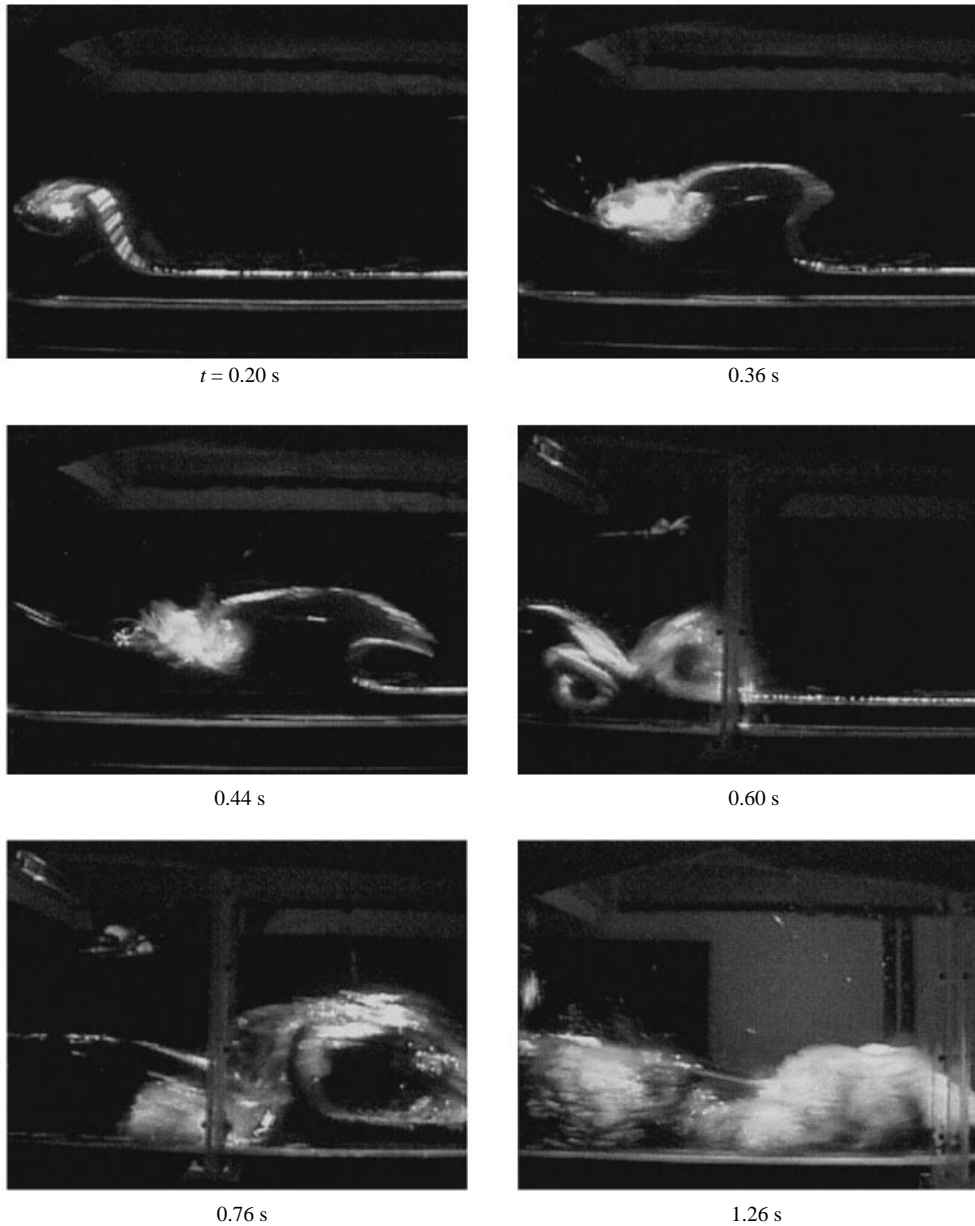
(*b*)

t = 0.20 s

0.36 s

0.44 s

0.60 s

0.76 s

1.26 s

FIGURE 2 (*b*). For caption see p. 412.

recorded at effectively 25 frames/sec and are digitized as 512×512 pixels with 256 grey levels through a frame grabber on a PC. Since the field of view unfortunately did not cover the entire flow area of interest, the camera had to be moved and the experiment repeated to obtain a complete visualization.

The free surface is obtained from the digitized images. The camera inevitably produces distortion. To correct this, a plane white board with a uniform square mesh printed on it is placed in the plane of the laser sheet with the flume empty and full
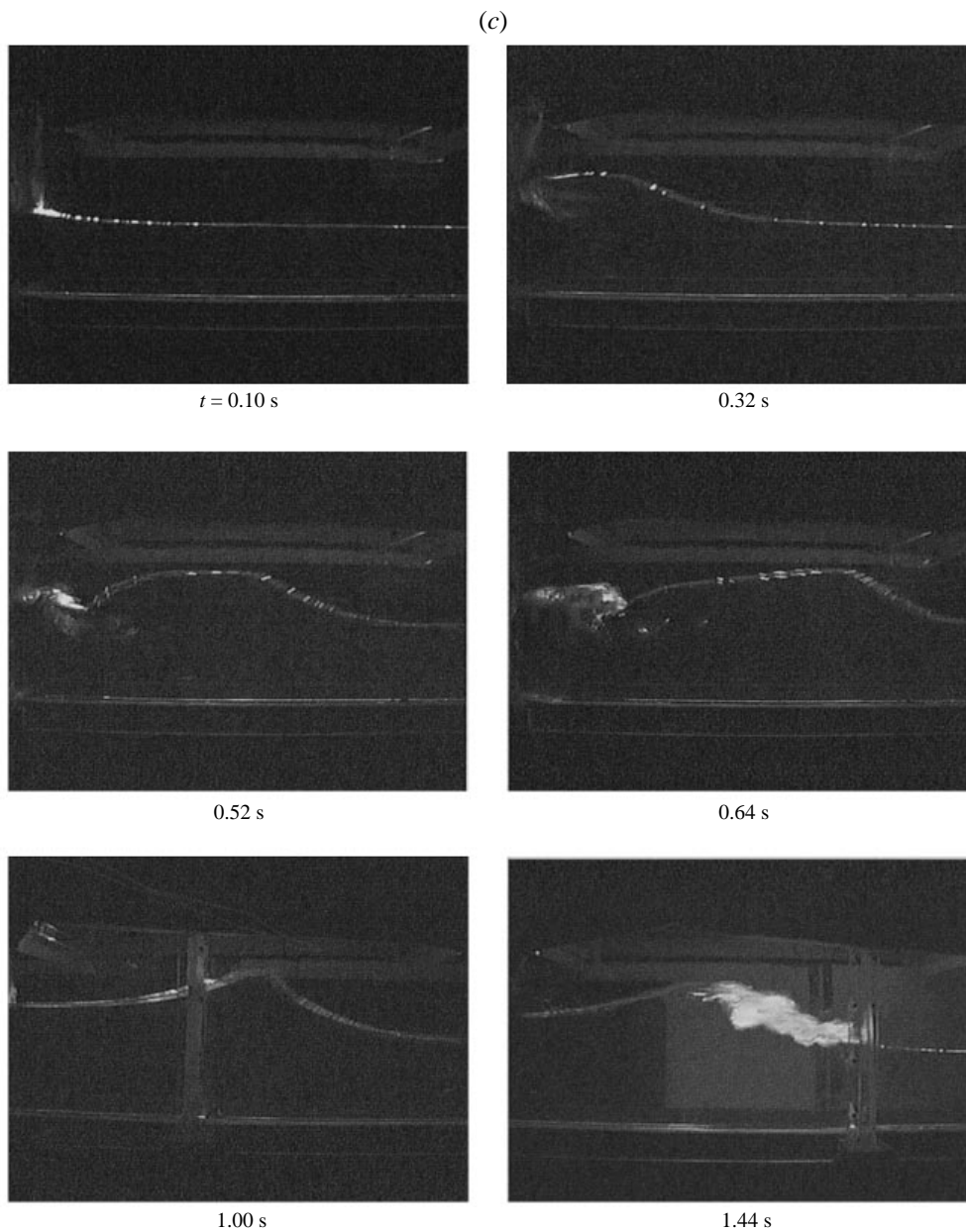
(*c*)

t = 0.10 s   0.32 s

0.52 s   0.64 s

1.00 s   1.44 s

FIGURE 2 (*c*). For caption see p. 412.

of water so that the distortion of the mesh may be quantified and any position in a video frame can thereafter be interpolated relative to the mesh. This takes account of refraction effects associated with water and Perspex. In this paper free-surface profiles only are presented. Velocity fields have also been produced by analysing successive images (the particle-image velocimetry method) and were particularly useful for investigating dam-break flows over obstacles (Chegini 1997). Surface elevations at various longitudinal positions were also measured using resistance probes and essentially confirmed the results from the video images.

(*d*)
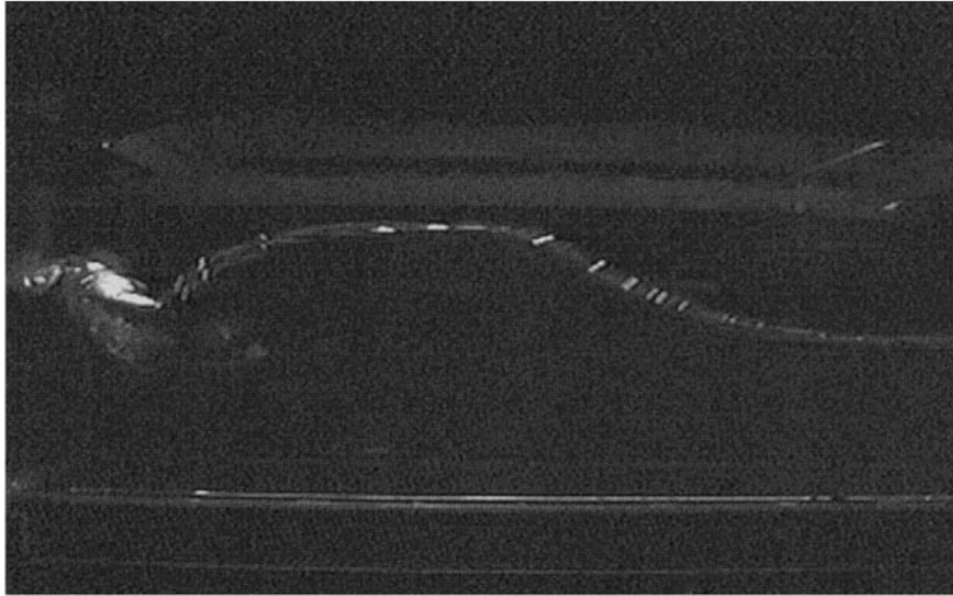
t = 0.52 s
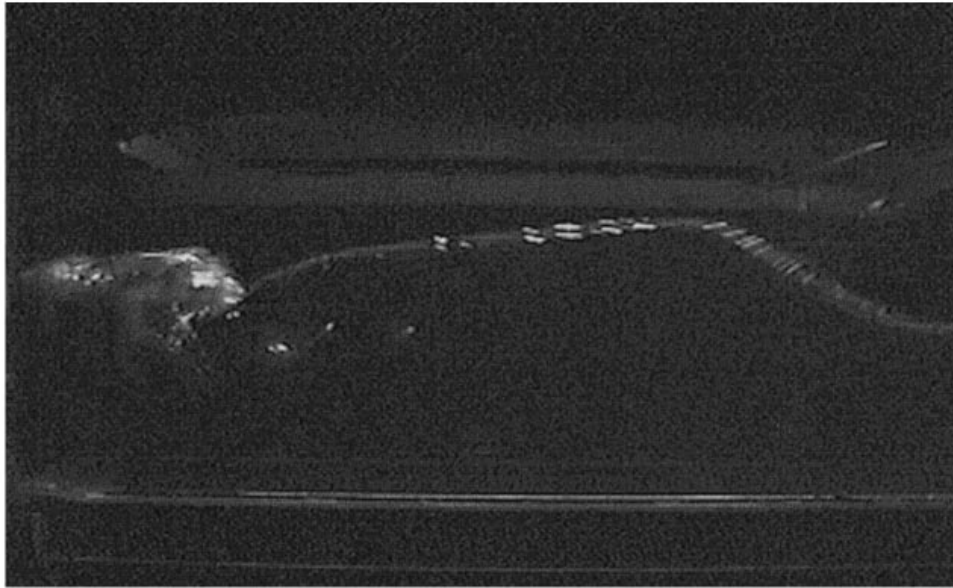
0.64 s

FIGURE 2. Digitized video images (untreated) at different times. (*a*) Dry-bed case. The first four images are with the camera just downstream of the dam, for the fifth the camera position is further downstream and for the sixth further downstream again. (*b*) Case with a depth ratio of 0.1. The camera is just downstream of the dam for the first three images, further downstream for the next two images and further downstream again for the last image. (*c*) Case with a depth ratio of 0.45. The camera is just downstream of the dam for the first four images, further downstream for the next image and further downstream again for the last image. (*d*) Enlargements of (*c*) at *t* = 0.52 and 0.64 s.
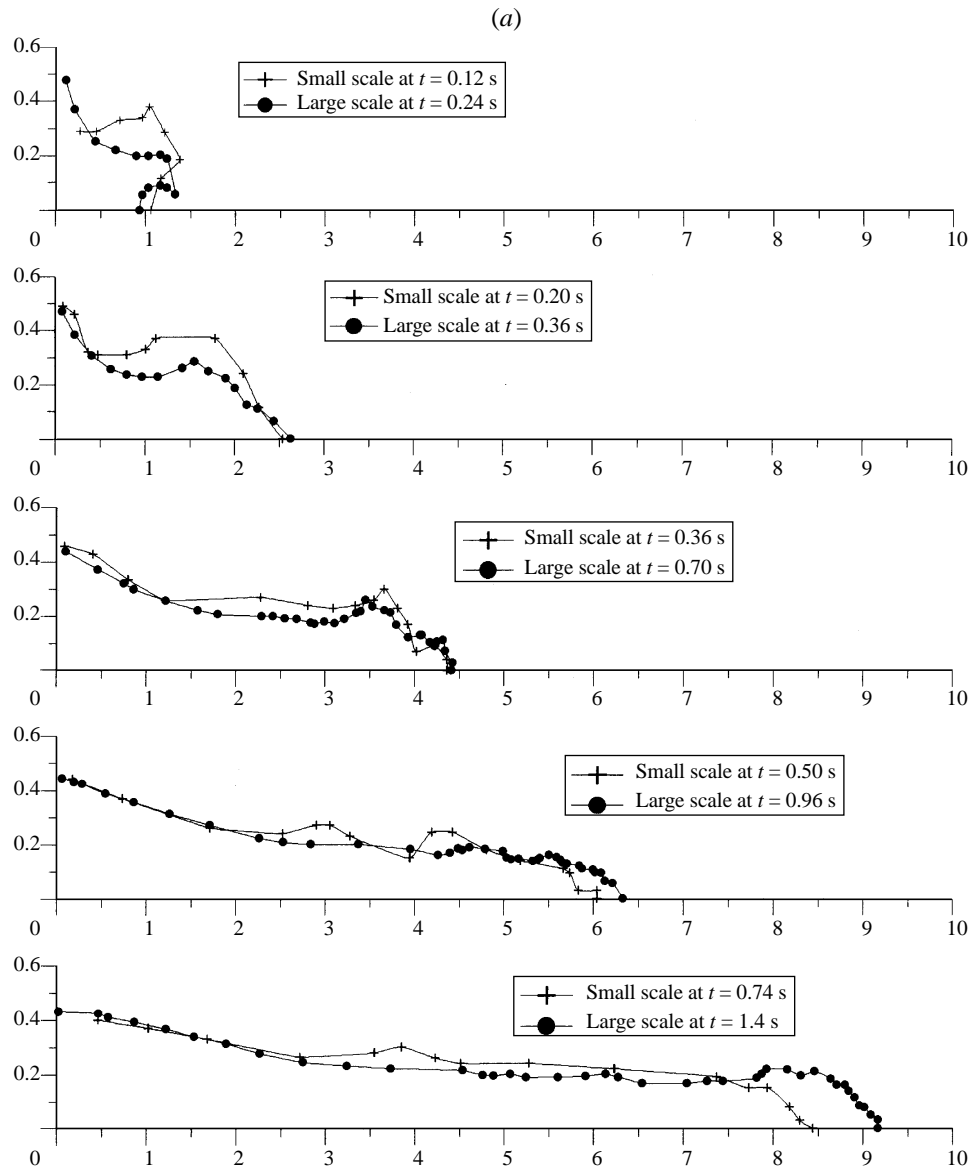
(*a*)

FIGURE 3 (*a*). For caption see p. 415.

The experiments were made at two scales: with upstream depths (η_0) of 0.1 m and 0.36 m and downstream depths of $0, 0.1\eta_0$, and $0.45\eta_0$ (depth ratios of 0, 0.1 and 0.45). If viscous and surface tension effects are negligible, the surface profiles should scale according to Froude criteria.

Figure 2(*a–d*) shows typical digitized images from the larger scale. The water surface is shown by the illuminated line. To aid illumination, Perspex powder is dropped on to the surface around the dam at the moment of its withdrawal and the powder is rapidly convected downstream. The laser sheet produces an illuminated line of finite thickness. This is usually quite thin before air entrainment occurs except in the region of jet formation at small times. It is not clear whether this is due to the finite sheet
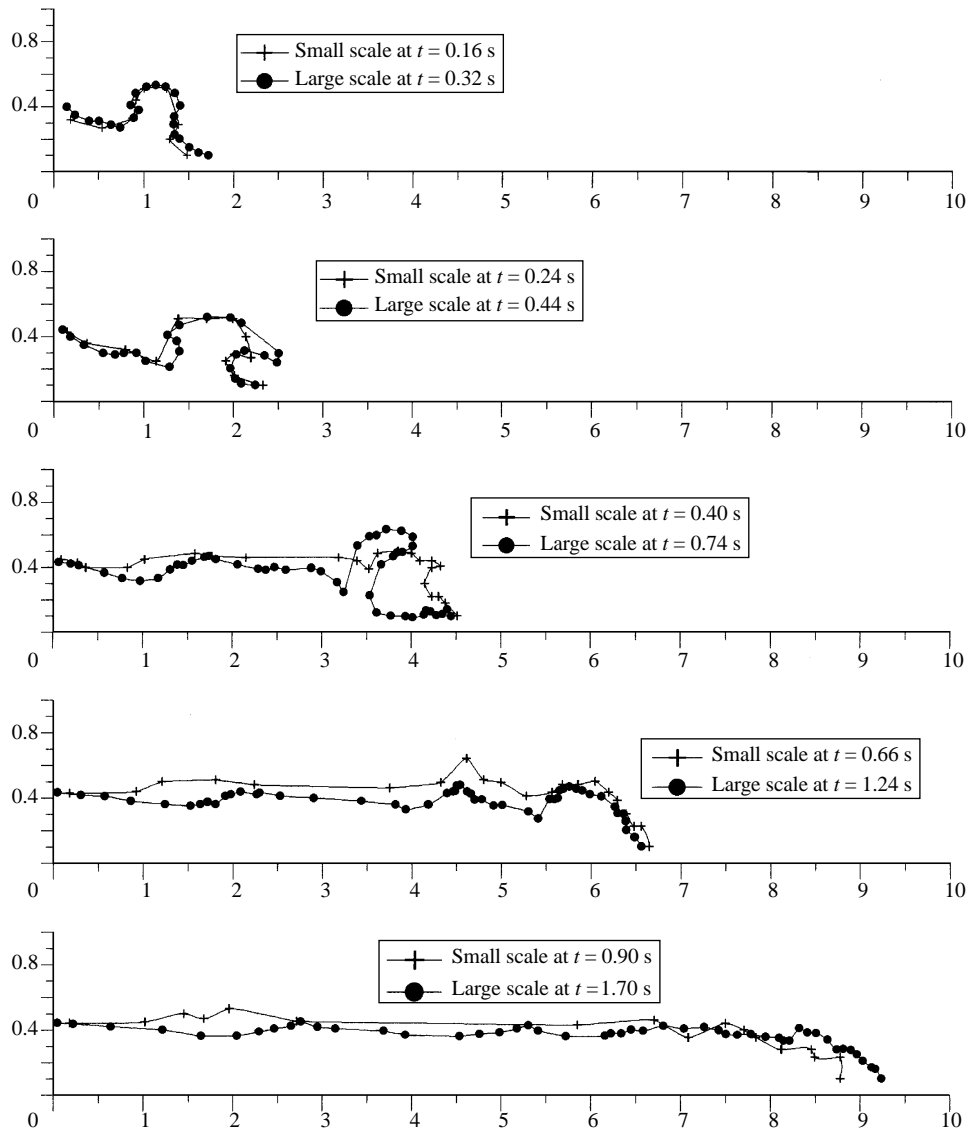
(*b*)

FIGURE 3 (*b*). For caption see facing page.

thickness or, more likely, digital noise associated with the high velocity in the jet. The surface is here defined by the inner limit of the illuminated line. This would coincide with the plane in the laser light sheet nearest to the camera if the sheet thickness causes the finite line thickness or with the start of the 'exposure' time. After the jet formation, the line is quite thin until water becomes aerated in the formation of a bore and the air bubbles reflect light. The water surface is then defined as the surface bounding the water/air mixture. Figure 2(*a*) shows results for the (nearly) dry-bed case; the first four images are with the camera just downstream of the dam, for the fifth the camera position is further downstream and for the sixth further downstream again. After a change in camera position the run was repeated. Figure 2(*b*) shows
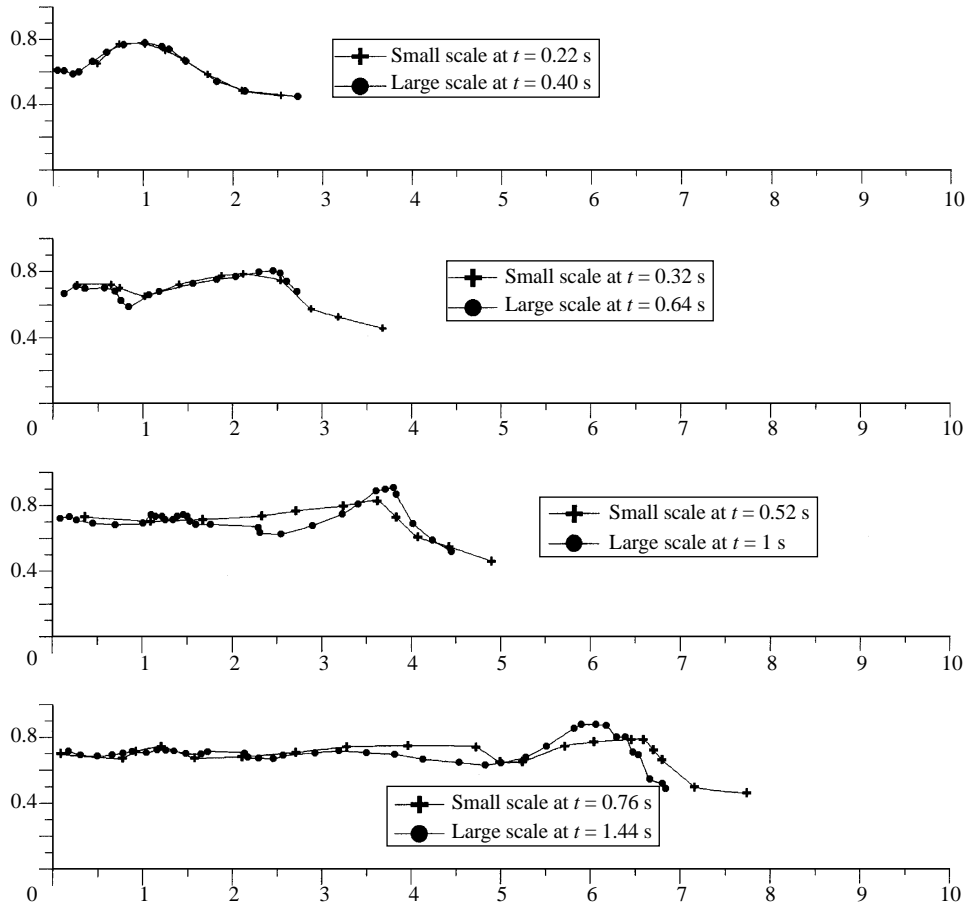
FIGURE 3. Profiles of maximum elevations obtained experimentally, normalized by η_0, for two scales (0.36 m and 0.1 m upstream depths) for a sequence of times. $x = 0$ corresponds to the dam site. (*a*) Dry-bed case. (*b*) Case with a depth ratio of 0.1. (*c*) Case with a depth ratio of 0.45.

results for the depth ratio of 0.1 where the camera is just downstream of the dam for the first three images, further downstream for the next two images and even further downstream for the last image. The light intensity just to the left of the mushroom jet appears particularly bright because the Perspex particles cluster as a result of the mushroom structure delaying their convection downstream. The video pictures suggest this region is in fact a mixture of spray and particles. Figure 2(*c*) shows results with a depth ratio of 0.45; here the camera is just downstream of the dam for the first four images, further downstream for the next image and still further downstream for the last time. Enlargements are shown in figure 2(*d*) for $t = 0.52$ and 0.64 s to show the mushroom-jet formation.

It is apparent from the video recordings that the plate is completely withdrawn from the flume in about 5 frames or 0.1 s. The time taken to be removed from the water will be rather less. The time origin $t = 0$ is defined as the instant when the plate leaves the bed. Figure 3 shows surface profiles with upstream depths η_0 of 0.1 m and 0.36 m, where the x, y-coordinates are normalized by η_0. If the Froude law is satisfied,
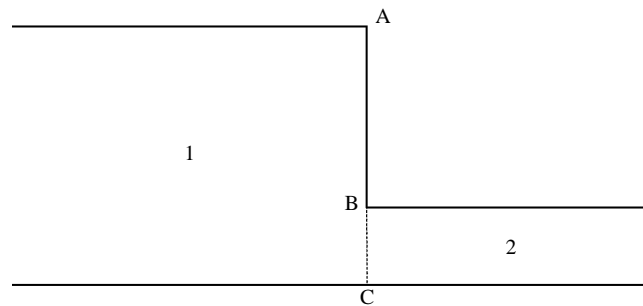
FIGURE 4. Definition sketch for initial-release analysis.

identical normalized profiles will occur when the ratio of the large-scale time to the small-scale time is $\sqrt{3.6} \approx 1.9$. This ratio is maintained as closely as possible when choosing frames for comparison. Figure 3(a) shows results for the dry-bed case and there are quantitative differences at all times. Although termed the dry-bed case, the downstream bed in fact has a thin film of water to a depth of 1–3 mm due to leakage. At the first time shown, a horizontal jet is formed at somewhat different positions for the two scales although in this case the time ratio is 2.0 (not 1.9). Thereafter, the general shape of the surge wave is quite similar at the two scales. It is possible that the finite time for plate withdrawal (less than 0.1 s) has some effect, particularly for very small times.

Figure 3(b) shows profiles with the depth ratio 0.1. Here a remarkable mushroom form erupts vertically with similar normalized dimensions at both scales. A forward jet is then produced which is clearly visible at the larger scale. It plunges forward into still water generating a further upward motion or splash, in the manner of a plunging breaker in a coastal engineering context. These latter formations are seen in the raw images of figure 2 but are not shown in the profiles which show the maximum surface elevation. This jet structure is not seen clearly at the smaller scale although the maximum elevations are quite similar.

Finally the case with a depth ratio of 0.45 is shown in figure 3(c). Here the profiles are quite similar at the two scales and, although a surge wave does not form downstream, figure 2(c) shows the formation of a wave which breaks, entraining air, having a similar form to what is known as a spilling breaker in a coastal engineering context. It appears from figure 2(c) and enlargements in figure 2(d) that a mushroom-like jet again forms just after the dam is withdrawn, as the large-scale downstream wave formation takes place.

3. Theory

3.1. *Initial release analysis*

We consider the release of an inviscid fluid which is initially stationary with two different water levels in regions 1 and 2, separated by a vertical sheet ABC, as shown in figure 4. At time $t = 0$, the sheet ABC is removed or dissolved instantaneously, causing an instantaneous adjustment of the pressure field since the fluid is incompressible. The pressure which was discontinuous on BC becomes continuous and the pressure on AB becomes constant (atmospheric). This adjustment of the pressure field causes the resulting unsteady motion, eventually producing a bore as observed experimentally.

We can compute the adjustment of the pressure field from the conservation equa-
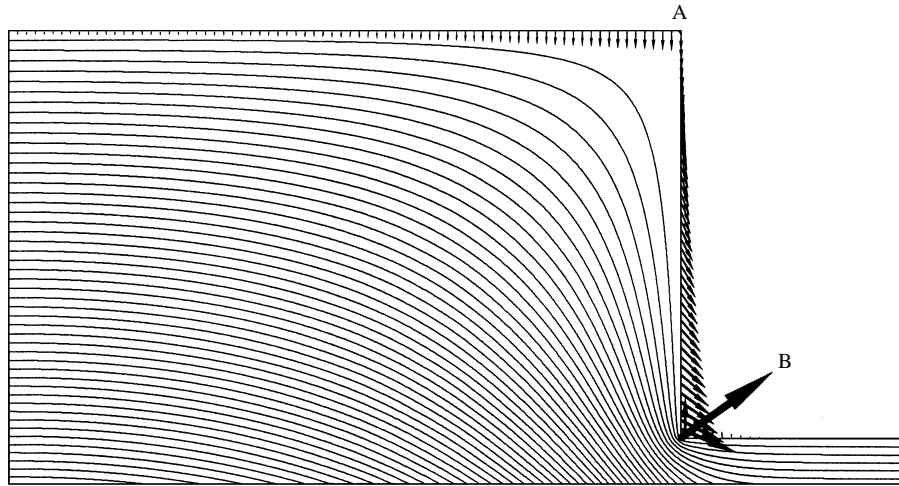
FIGURE 5. Pressure contours within the fluid at the time of release, and acceleration vectors on the surface, with the arrow length proportional to magnitude. For corner B this magnitude is theoretically infinite. The depth ratio is 0.1.

tions for mass and momentum. In regions 1 and 2, p_1 and p_2 are the hydrostatic pressures before the sheet is dissolved. Just after the sheet is dissolved, since the velocities are zero at $t = 0$, the momentum equations become

$$\frac{\partial}{\partial t}(\nabla \phi_1) = -\frac{1}{\rho}\nabla p_1 + \boldsymbol{g}, \tag{1}$$

$$\frac{\partial}{\partial t}(\nabla \phi_2) = -\frac{1}{\rho}\nabla p_2 + \boldsymbol{g}, \tag{2}$$

where $\phi = \phi(\boldsymbol{x}, t)$ is velocity potential, $\boldsymbol{x} = (x, y)$ and $\boldsymbol{g} = (0, -g)$, g being the acceleration due to gravity. Taking the divergence of these equations,

$$\nabla^2 p_1 = 0, \tag{3}$$

$$\nabla^2 p_2 = 0 \tag{4}$$

since $\nabla^2 \phi_1 = 0, \nabla^2 \phi_2 = 0$.

The boundary conditions may be given by $p_2 = p_1 = 0$ along the free surface, $\partial p_1 / \partial x = \partial p_2 / \partial x$ on the interface between 1 and 2 (BC), ensuring the velocity normal to this interface is continuous across it, and $\partial p_1 / \partial y = \partial p_2 / \partial y = -\rho g$ along the horizontal bed. At large distances from the interface the pressure change is negligible due to release at $t = 0$ and we set $\partial p_1 / \partial x = \partial p_2 / \partial x = 0$.

We may now solve $\nabla^2 p = 0$ (omitting suffices 1 and 2) and pressure contours are shown in figure 5 for the depth ratio of 0.1. There is clearly a singularity at the corner B. The results shown were obtained numerically on a uniform mesh using a finite-difference approximation. There are similar results for depth ratios of 0 and 0.45.

The flow accelerations are given by (1), (2) and vectors are shown on the surface by the arrows in figure 5. Note that the arrow from corner B is theoretically of infinite length due to the singularity. The surface at corner A falls vertically with gravitational acceleration alone and the surface at large distances from the interface remains stationary.

A singularity is of course physically impossible but this analysis indicates that there will be jet formation at B. The flow development for small time may be considered

further by artificially removing the singularity by smoothing the corner at B and computing the fully nonlinear, potential flow with a free surface.

3.2. *Nonlinear potential-flow theory for small times*

The potential flow with a free surface at constant pressure (set to zero) in a vertical plane may be described by the velocity potential ϕ, which satisfies the following equations:

in the fluid

$$\nabla^2 \phi = 0, \tag{5}$$

on the free surface

$$\frac{\mathrm{D}x}{\mathrm{D}t} = \nabla \phi, \tag{6}$$

$$\frac{\mathrm{D}\phi}{\mathrm{D}t} = \tfrac{1}{2} \mid \nabla \phi \mid^2 - g\eta, \tag{7}$$

and on the bed

$$\frac{\partial \phi}{\partial y} = 0, \tag{8}$$

where $\mathrm{D}/\mathrm{D}t$ is the total derivative. The bed is treated as a plane of symmetry and there is no flow at the vertical surfaces defining the ends of the computational domain.

An accurate numerical method for the solution of this problem is described in Cooker *et al.* (1990), developed from the method of Dold & Peregrine (1986), see also Dold (1992). The flow is described as a boundary-integral problem where particle positions on the free surface and their velocity potential are advanced in time. The points may be arbitrarily chosen and clustered around regions where high distortion is expected in order to give high accuracy. Cauchy's integral theorem is applied to the complex velocity on the surface. The resulting integrals are of principal-value form with singular parts and the non-singular parts are obtained using the trapezoidal rule. The horizontal bed is represented by adding the image of the surface in the bed. Time advancement is described by a fifth-order Taylor series. The method requires a 'smooth' surface and breaks down if the curvature at any point becomes too great for accurate numerical resolution.

Figure 6(*a*) shows the results from the computations with a thin layer of water downstream. The very small water depth rather than a dry bed was necessary in the numerical scheme. To avoid right angles at the changes in surface level an initial shape of the form

$$\frac{\eta}{\eta_0} = 0.01 + 0.5(1 - \tanh(kx/\eta_0)) \tag{9}$$

is used. Results with $k = 10$ are shown in figure 6(*a*) up to the time when the surface curvature becomes so great at the outer 'corners' of the jet that the solution breaks down. Reducing k made this time larger and increasing k made it smaller. The profiles all show a horizontal jet qualitatively similar to those seen in the experiments.

Figure 6(*b*) shows results with a depth ratio of 0.1. In this case the initial profile is smoothed by replacing the right angles at the intersections of the horizontal and vertical surfaces by circular arcs of radius $0.1\eta_0$. Reducing the radius decreased the time at which the surface curvature becomes so large that the solution breaks down and increasing the radius increased this time. An upward mushroom-like jet is clearly seen, qualitatively similar to that observed experimentally.
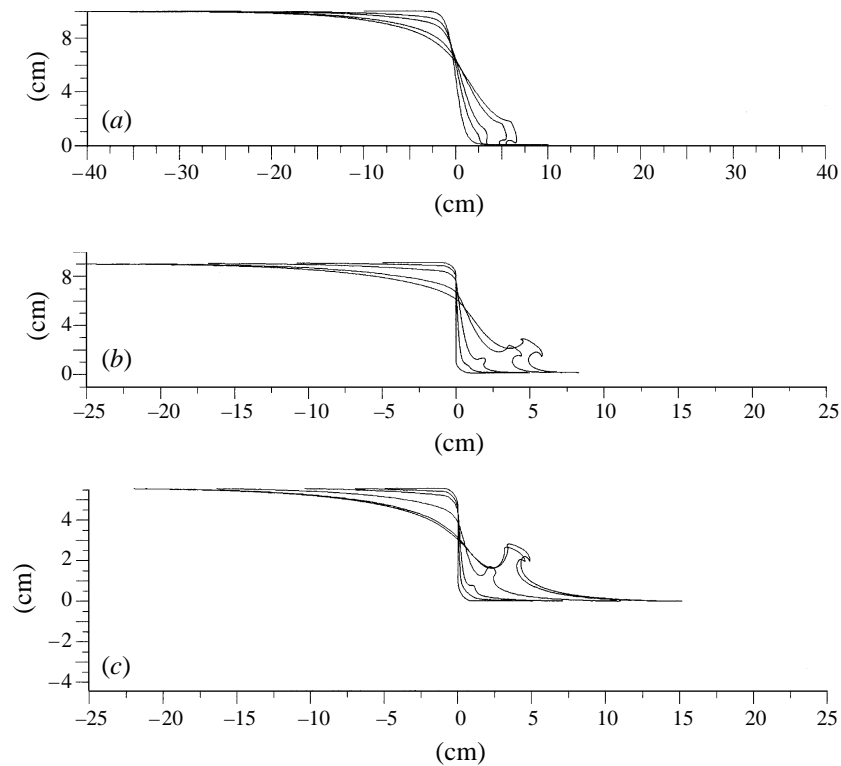
FIGURE 6. Profiles of surface elevation from nonlinear potential-flow computations, with the upstream depth (0.1 m) of the small-scale experiment. (*a*) Dry-bed case (downstream depth of $0.01\eta_0$) at succesive times of 0, 0.036, 0.05, 0.074, 0.085 s. (*b*) Case with a depth ratio of 0.1 at successive times of 0, 0.024, 0.04, 0.066, 0.08 s. (*c*) Case with a depth ratio of 0.45 at successive times of of 0, 0.02, 0.03, 0.052, 0.076, 0.08 s.

For the depth ratio of 0.45 with the same circular-arc smoothing, an initial jet structure is shown in figure 6(*c*), again similar to that observed experimentally.

3.3. *Shallow-water theory*

With the assumption of hydrostatic pressure, the Navier–Stokes/continuity equations with a free surface reduce to the shallow-water equations. It is further assumed that the velocity is uniform over depth. Following Stoker (1957) the two-dimensional vertical plane problem becomes a one-dimensional problem and for a horizontal bed ignoring friction the mass and momentum conservation equations are given by

$$\frac{\partial \eta}{\partial t} + \frac{\partial}{\partial x}(u\eta) = 0, \tag{10}$$

$$\frac{\partial u}{\partial t} + u\frac{\partial u}{\partial x} = -g\frac{\partial \eta}{\partial x}, \tag{11}$$

where η is water surface elevation above the bed and u is the velocity in the *x*-direction. The equations may be written

$$\left[(u \pm c)\frac{\partial}{\partial x} + \frac{\partial}{\partial t}\right](u \pm 2c) = 0, \tag{12}$$

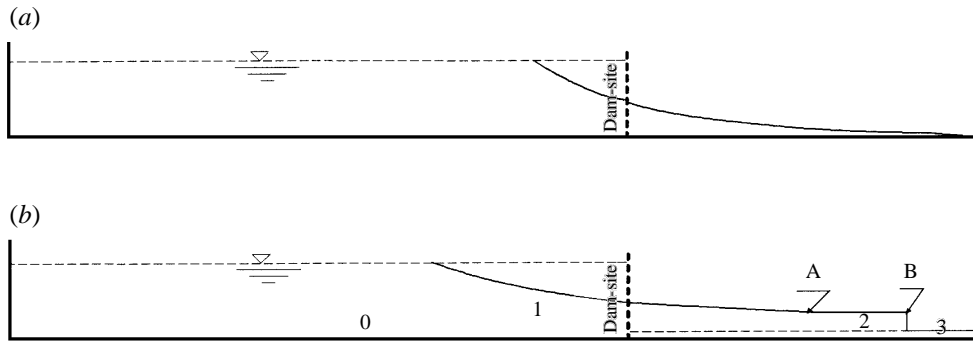where $c = (g\eta)^{1/2}$ and the Riemann invariants $(u \pm 2c)$ are constant.

(*a*)

(*b*)

FIGURE 7. Typical profiles from the shallow-water equations: (*a*) dry-bed downstream, (*b*) with water downstream.

First, we consider the simplest analytical case of a dry bed (zero depth) downstream of a depth η_0 where the initial condition and a later elevation profile are shown in figure 7(*a*). A negative wave is produced and the movement of a moving point is described by the backwards characteristic

$$\frac{\mathrm{d}x}{\mathrm{d}t} = u - c, \tag{13}$$

and the constant value of the forward Riemann invariant is given by the initial condition ($t = 0$)

$$u + 2c = 2c_0, \tag{14}$$

where $c_0 = (g\eta_0)^{1/2}$.

Since the characteristic is a straight line we have the simple relation in the region of wave propagation

$$x = \left[2(g\eta_0)^{1/2} - 3(g\eta)^{1/2}\right] t. \tag{15}$$

With non-zero depth downstream the problem is a little more complicated. Equation (15) still applies upstream but there is also a bore travelling downstream into the still water region as shown in figure 7(*b*), where the different flow regimes are numbered. A physical constraint defining the bore is that velocity is continuous at the boundary between regions 1 and 2 where the elevation is also continuous. At this boundary (A) from region 1

$$u_A = 2c_0 - 2(g\eta_A)^{1/2} \tag{16}$$

and u_A is thus the value for region 2. Constant mass flux must also be maintained across the bore (position B) advancing with speed c_B giving

$$-c_B\eta_3 = (u_A - c_B)\eta_A \tag{17}$$

where $\eta_A = \eta_B = \eta_2, u_A = u_2$, and with the equation for a bore moving into still water

$$\frac{c_2^2}{c_3^2} = \frac{\eta_A}{\eta_3} = \frac{1}{2}\left[\left(1 + 8\frac{c_B^2}{c_3^2}\right)^{1/2} - 1\right] \tag{18}$$

the situation is defined and may be solved in an iterative procedure. Substituting for c_B and u_A gives η_A/η_3 which is independent of time.
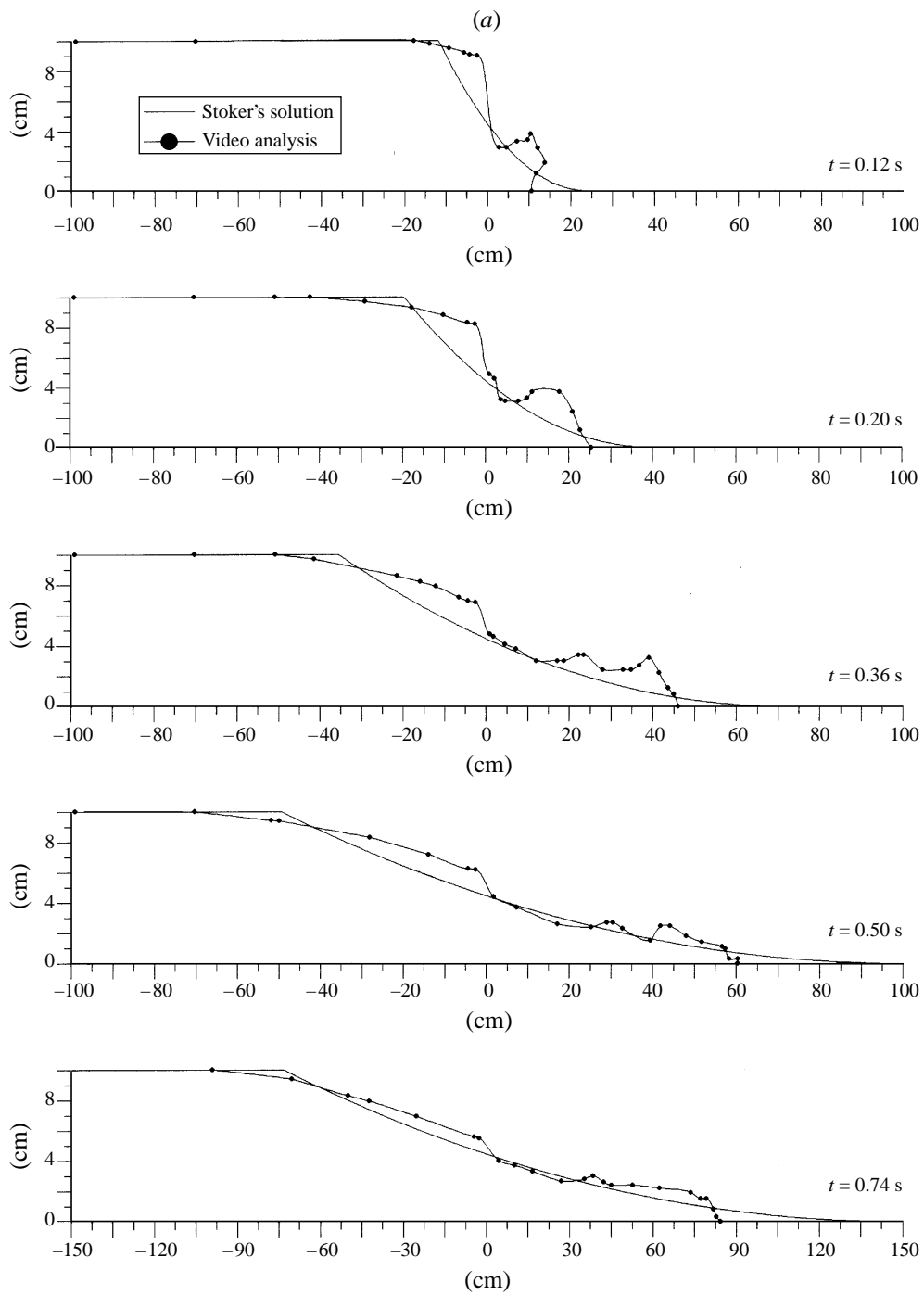
(*a*)

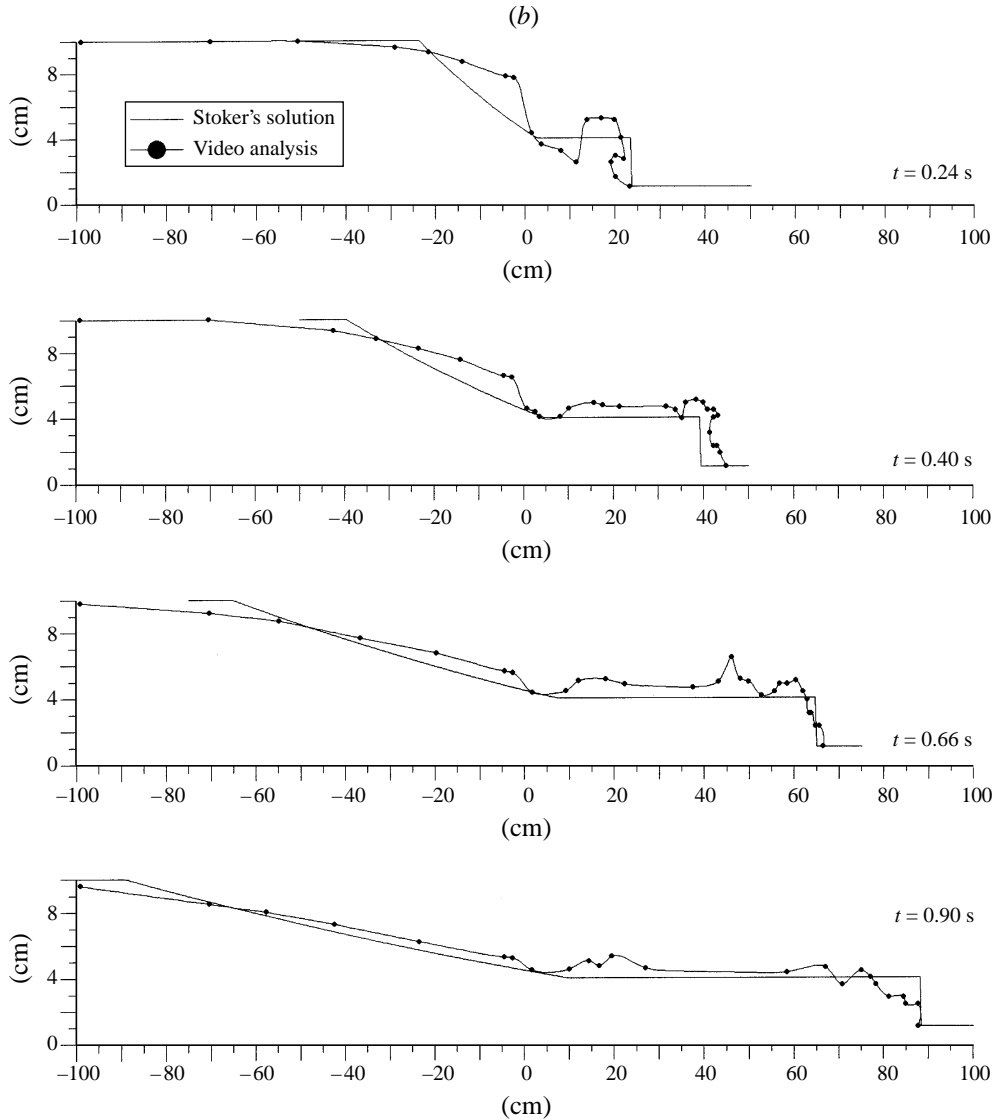FIGURE 8 (*a*). For caption see p. 423.

FIGURE 8 (*b*). For caption see facing page.

The depth at the dam site is constant at $\frac{4}{9}\eta_0$ provided the downstream depth is less than $0.1384\eta_0$ and otherwise is constant at a greater value.

Comparisons with experimental profiles are shown in figure 8(*a–c*) for the smaller scale (since the time of plate withdrawal above the water level is smaller and air entrainment appears rather less than at the larger scale). For all depth ratios, while the differences at small times are substantial, the profiles eventually become quite similar after the bore has developed downstream. The experimental profiles show the upper limit of the flow including the air/water mixture since this can be simply measured.

The influence of friction was investigated in a numerical simulation and was found to have an insignificant effect on the results.
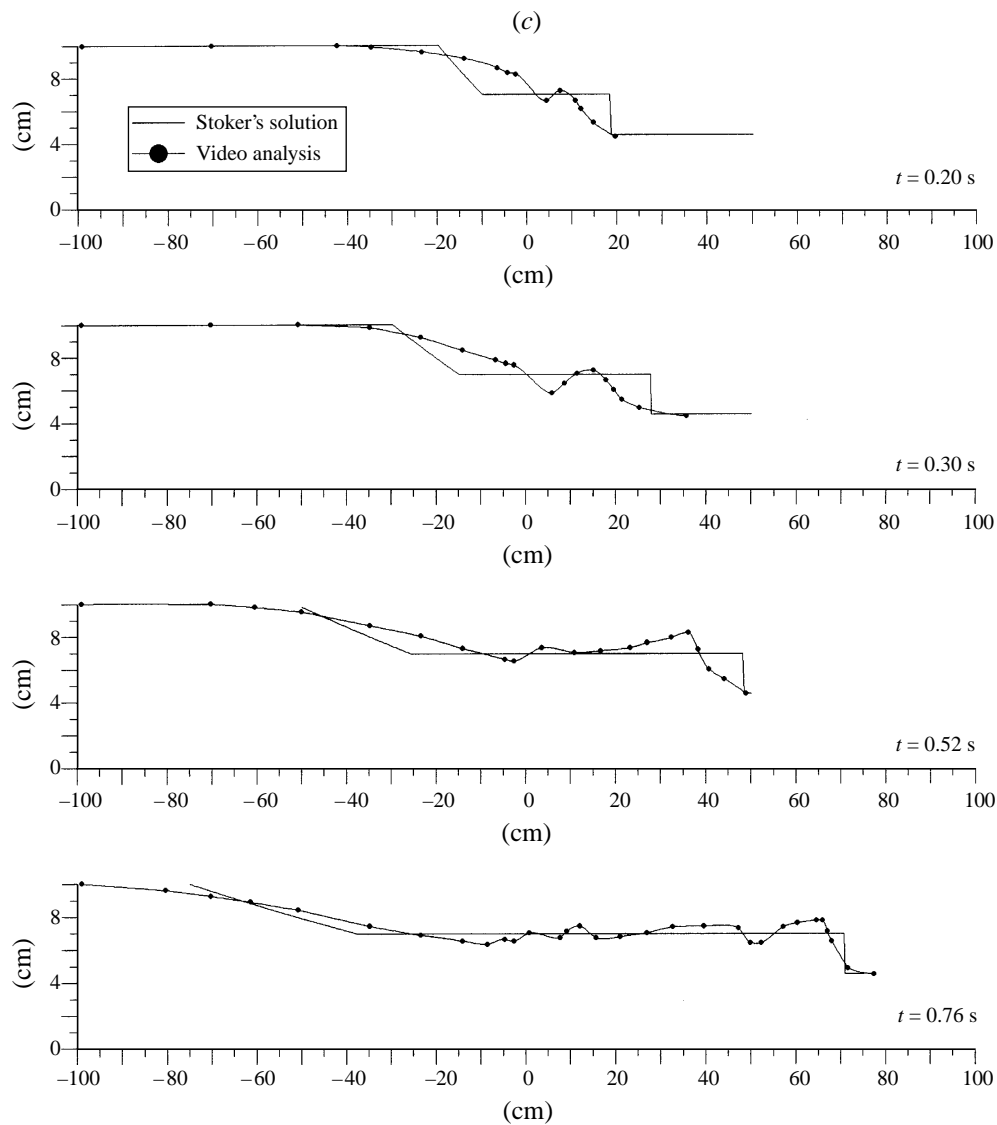
FIGURE 8. Profiles of maximum elevation for the smaller-scale experiment (dimensions in cm) with solutions of the shallow-water equations for a sequence of times. (*a*) Dry-bed case. (*b*) Case with a depth ratio of 0.1. (*c*) Case with a depth ratio of 0.45.

4. Conclusions

Experiments on dam-break flow have shown some new jet-like phenomena just after release. These features are consistent with analysis for the time of release and, for small times afterwards, are reproduced qualitatively in highly accurate, nonlinear, potential-flow computations with artificially-smoothed, initial surface profiles. In the experiments the jets interacted with the bed or the downstream water in a highly complex manner, entraining air, but after a bore (or spilling breaker) had become established the profiles showed quite close agreement with analytical solutions of the shallow-water equations.

REFERENCES

CHEGINI, A. 1997 Fundamental investigations of dam-break flows. PhD dissertation, University of Manchester.

COOKER, M. J., PEREGRINE, D. H., VIDAL, C. & DOLD, J. W. 1990 The interaction between a solitary wave and a submerged circular cylinder. *J. Fluid Mech.* **215**, 1–22.

DOLD, J. W. 1992 An efficient surface-integral algorithm applied to unsteady gravity waves. *J. Comput. Phys.* **103**, 90–115.

DOLD, J. W. & PEREGRINE, D. H. 1986 An efficient boundary integral method for steep unsteady water waves. In *Methods for Fluid Dynamics II* (ed. K. W. Morton & M. J. Baines), pp. 671–679. Oxford University Press.

HARLOW, F. H. & WELCH, J. E. 1965 Numerical calculation of time-dependent viscous incompressible flow of fluid with a free surface. *Phys. Fluids* **8**, 2182–2189.

HIRT, C. W. & NICHOLS, B. D. 1981 Volume of fluid (VOF) method for the dynamics of free boundaries. *J. Comput. Phys.* **39**, 201–225.

NICHOLS, B. D. & HIRT, C. W. 1971 Improved free surface conditions for numerical incompressible flow computations. *J. Comput. Phys.* **8**, 434–448.

STOKER, J. J. 1957 *Water Waves.* Interscience.